

Chapter 1

Point Source Digital In-Line Holographic Microscopy

Manfred H. Jericho and H. Jürgen Kreuzer

Abstract Point source digital in-line holography with numerical reconstruction has been developed into a new microscopy, specifically for microfluidic and biological applications, that routinely achieves both lateral and depth resolution at the submicron level in 3-D imaging. This review will cover the history of this field and give details of the theoretical and experimental background. Numerous examples from microfluidics and biology will demonstrate the capabilities of this new microscopy. The motion of many objects such as living cells in water can be tracked in 3-D at subsecond rates. Microfluidic applications include sedimentation of suspensions, fluid motion around micron-sized objects in channels, motion of spheres, and formation of bubbles. Immersion DIHM will be reviewed which effectively does holography in the UV. Lastly, a submersible version of the microscope will be introduced that allows the in situ study of marine life in real time in the ocean and shows images and films obtained in sea trials.

1.1 Introduction

In the late 1940s, more than a decade after Ernst Ruska had invented the electron microscope, the main obstacle for its practical implementation was the fact that magnetic electron lenses were far from ideal showing substantial aberration effects. Compared to optical glass lenses they had the quality of the bottom of a champagne bottle. It was then that Dennis Gabor [1] came up with the idea that one should get rid of magnetic electron lenses altogether and use the only “perfect” lens available, that is a pinhole or point source of a size less than or about a wavelength. From such a point source a spherical wave emanates within a cone of half angle θ given by the numerical aperture NA of a hole

$$n \sin \theta = \text{NA} = 0.62 \frac{\lambda}{r} \quad (1.1)$$

H.J. Kreuzer (✉)

Department of Physics and Atmospheric Science, Dalhousie University, Halifax,
NS B3H 3J5 Canada

e-mail: H.J. kreuzer@DAL.CA; kreuzer@Fizz.Phys.dal.ca

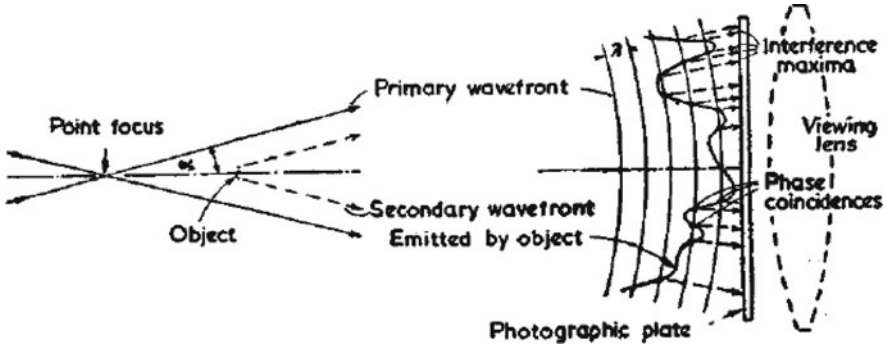


Fig. 1.1 The geometry of holography with a point source in Gabor's Nature paper

where λ is the wavelength of the radiation illuminating the pinhole and r is its radius. Such a point source has the additional advantage that the emanating radiation originates at the same point in space, i.e., it is spatially coherent. Moreover, it is an expanding wave, i.e., it has perfect magnification built in. Gabor's original drawing is reproduced in Fig. 1.1.

Holography in this geometry should be termed more concisely as Point Source In-line Holography to set it apart from Parallel or Collimated Beam In-line Holography advanced after the invention of the laser in the 1960s [2, 3]. Unfortunately, this distinction is often blurred to the extent that in a popular textbook [4] on holography the Collimated Beam geometry is presented as Gabor's original idea. This review is solely concerned with point source in-line holography, and apart from a few historical remarks on electron holography it is exclusively dealing with light as the primary source of radiation. A schematic more suited for the present work is given in Fig. 1.2.

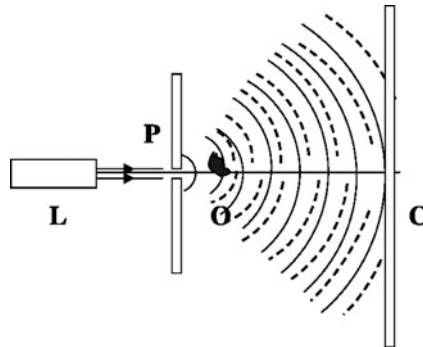


Fig. 1.2 Schematic of DIHM: A laser L is focused onto a pinhole P. The emerging *spherical* wave illuminates the object O and the interference pattern or hologram is recorded on the screen C. The *solid* and *dashed* lines are reference and scattered wave, respectively

The light emanating from the point source is propagating to the screen with some of it being scattered by the object in front of the source. Thus the wave amplitude at the screen is given by

$$A(\mathbf{r}) = A_{\text{ref}}(\mathbf{r}) + A_{\text{scat}}(\mathbf{r}) \quad (1.2)$$

and the intensity recorded on the screen becomes

$$\begin{aligned} I(\mathbf{r}) &= A(\mathbf{r})A^*(\mathbf{r}) \\ &= A_{\text{ref}}(\mathbf{r})A_{\text{ref}}^*(\mathbf{r}) + [A_{\text{ref}}(\mathbf{r})A_{\text{scat}}^*(\mathbf{r}) + A_{\text{scat}}(\mathbf{r})A_{\text{ref}}^*(\mathbf{r})] + A_{\text{scat}}(\mathbf{r})A_{\text{scat}}^*(\mathbf{r}) \end{aligned} \quad (1.3)$$

The first term on the right is the intensity of the unscattered part of the reference wave; the last term is the intensity of the scattered wave; it is the subject of classical diffraction theory in wave optics. The two terms in the square bracket represent the interference between the reference and the scattered waves. This is called holographic diffraction and is the basis of holography.

When are classical or holographic diffraction and interference dominant? Obviously if the object blocks out most of the reference wave the scattered wave can only interfere with itself if sufficiently coherent; a double slit configuration is a case in point. Another example is a simple pinhole camera. In the latter the radius of the pinhole is typically many times the wavelength to allow more light to get into the camera chamber. Sunlight or a lamp illuminates the front of the object, and the reflected light enters the pinhole incoherently. The reference wave (sun or lamp) does not contribute directly to the image inside the camera.

On the other hand, if the object blocks out only a small part of the reference wave holographic diffraction is dominant and leads to a complicated interference pattern on the screen. The fact that the holographic intensity is linear in the scattering amplitude has two important mathematical consequences: (1) the superposition principle holds, i.e., adding two or many holograms does not lead to a loss of information as it would for classical optics where double exposure of a photographic film in a pinhole camera surely reduces or even destroys the information and (2) the scattering amplitude recorded in the hologram can be traced back to the scattering object and extracted including its phase. This is essentially the reason why, by an inverse procedure, one can extract the wave front anywhere at the object thus creating a 3-D image of the object from a 2-D recording on the screen. How is this achieved?

There are two ways of back propagating a wave through a hologram: experimentally and theoretically. Experimentally Gabor's idea was to record or transfer the (electron) hologram onto a semi-transparent film (photographic negative, for instance) and illuminate it from the back with a spherical converging wave. There are three problems with this approach:

(a) it is difficult to produce a large enough spherical wave with a lens without encountering aberration effects; (b) the resulting image as viewed through the hologram is its original size, i.e., no magnification has been achieved; thus this is

not a microscope; and (c) when looking at the object image through the hologram one looks straight into the point source reproduced by the converging wave, i.e., no object is visible, it is as invisible as a plane when it flies across the sun.

Gabor's solution to get magnification was simple: take a hologram with electrons of wavelength less than 1 Å, i.e., energies in excess of 100 eV. Then magnify the hologram mechanically by a factor of 5000 and use visible light of the appropriate wavelength to illuminate it. Magnification is now 5000-fold. To avoid the problems with Gabor's geometry of point source holography various schemes of off-line or off-axis holography have been developed [2–5] that rely on parallel light beams as generated by lasers but this is not the topic of this review.

A much easier way to do the back propagation is numerically already contemplated by Gabor [6]. Early implementations of numerical reconstruction were frustrated by the need of simplifications of the reconstruction formula due to the lack of computer power [7–12]. The development of a fast and efficient reconstruction algorithm in the 1990s leads to the emergence of DIHM – Digital In-line Holographic Microscopy as tool for 4-D imaging with submicron length and subsecond timescales of the time-dependent trajectories of microscopic objects in 3-D space [13]. Unlike conventional compound light microscopy, which can give high-resolution information about an object only in the focal plane with a depth of field of less than a micron, digital in-line holographic microscopy (DIHM) offers a rapid and efficient approach to construct high-contrast 3-D images of the whole sample volume from a single hologram.

In-line point source holography with electrons was revived in the late 1980s by Fink et. al. [14–19] when they managed to make stable field emission tips that ended in a single atom thus creating an intense point source for coherent electrons in the energy range from roughly 10 to 300 eV, i.e., for wavelengths from 2 down to 0.5 Å. High-resolution holograms were recorded digitally using a CCD camera and a theory was developed for the numerical reconstruction of these holograms [16, 17]. This must be considered the first success of digital in-line holography with electrons [20–23]. Although the reconstruction algorithm was originally designed for electron holography, its transfer to optical holography is straightforward [24–27].

1.2 DIHM Hardware

DIHM hardware is very simple as illustrated in Fig. 1.2: A low-power laser **L** is focused on a pinhole **P** of typically 1 μm in diameter from which the spherical reference wave emerges. Using a laser diode this light source can be assembled in a standard lens holder which serves as an holographic add-on to any standard microscope. For high-resolution work the object **O** is placed less than 1 mm from the pinhole and the CCD camera **C** is adjusted in position to record the entire emission cone of the pinhole. If only resolution of several microns is required then a larger pinhole of several microns in diameter can be used and the larger sample is placed further from

the pinhole. The CCD camera (physical size and pixel number) must be chosen to satisfy the Nyquist–Shannon criteria to avoid aliasing in the reconstruction.

1.3 Hologram Reconstruction

As outlined above, holography is a two-stage process. First a hologram is taken and stored digitally. Second, the role of reconstruction in holography is to obtain the 3-D structure of the object from the 2-D hologram on the screen, or, in technical terms, to reconstruct the wave front at the object. In DIHM this is done numerically based on the theory of wave propagation in optics, i.e., by backward diffraction of the digitally stored pattern on the 2-D hologram via the reference wave. This diffraction process is given in scalar diffraction theory by the Kirchhoff–Fresnel transform:

$$K(\mathbf{r}) = \int_{\text{screen}} \tilde{I}(\boldsymbol{\xi}) A_{\text{ref}}(\boldsymbol{\xi}) \frac{\exp[-ik|\boldsymbol{\xi} - \mathbf{x}|]}{|\boldsymbol{\xi} - \mathbf{x}|} F_{\text{in}}(\boldsymbol{\xi}) d\boldsymbol{\xi} \quad (1.4)$$

Here

$$\tilde{I}(\boldsymbol{\xi}) = I(\boldsymbol{\xi}) - A_{\text{ref}}(\boldsymbol{\xi}) A_{\text{ref}}^*(\boldsymbol{\xi}) \quad (1.5)$$

is the contrast intensity, \mathbf{x} and $\boldsymbol{\xi}$ are vectors from the point source to the object and screen, respectively, $k = 2\pi/\lambda$ is the inverse wave number and χ is the angle between the optical axis from the point source to the center of the screen a distance L away, and the vector $\boldsymbol{\xi}$ on the screen. For a point source the reference wave is spherical, i.e., $A_{\text{ref}}(\boldsymbol{\xi}) = \xi^{-1} \exp[-ik\xi]$. Thus Fresnel's approximation to the inclination factor becomes (for the geometry in which the screen is perpendicular to the optical axis)

$$F_{\text{in}}(\boldsymbol{\xi}) = -\frac{i}{2\lambda}(1 + \cos \chi) = -\frac{i}{2\lambda} \left(1 + \frac{L}{\xi}\right) \quad (1.6)$$

Taking the contrast intensity is convenient and advantageous as it removes any unwanted flaws and imperfections in the laser illumination. In addition, by subtracting the laser intensity at the screen in the absence of the object one eliminates this dominant term and also, more importantly, any flaws in the laser or camera. This subtraction can be done as just outlined or, if the removal of the object is not practical, one applies a high-pass filter to the hologram.

$K(\mathbf{r})$ is a complex wave amplitude that can be calculated according to (1.4) anywhere in space, in particular in the volume of the object/sample, thus rendering its 3-D structure if sufficiently transparent. The absolute square $|K(\mathbf{r})|^2$ yields the intensity at the object and its phase gives information about its index of refraction. The numerical evaluation of the diffraction integral is very time consuming even for a “small” hologram of only $10^3 \times 10^3$ pixels. Observing that the Kirchhoff–Fresnel integral is a convolution one is tempted to use fast Fourier

transforms for its evaluation. To do this one needs to digitize (1.4) as the hologram itself is of course given in digitized form, $\xi \rightarrow (\nu, \mu)a$ where ν and μ enumerate the pixels on the CCD chip and a is the pixel size. Likewise, one needs to digitize the space coordinates $\mathbf{r} \rightarrow (nb, mb, z)$, where b is the size of one pixel in the reconstructed image. Unfortunately, to keep the digitized form of (1.4) a convolution one needs to make the identification $b = a$ thus eliminating the opportunity to obtain a magnified image of the object or to use point source DIHM as a viable microscopic technique. To overcome this impasse we explore possibilities to simplify the diffraction integral itself. We observe that in DIHM the distance from the pinhole to the object is typically much smaller than to the screen. Thus we can use an expansion

$$|\xi - \mathbf{x}| \approx \xi \left[1 - \frac{2\xi \cdot \mathbf{x}}{\xi^2} \right]^{1/2} \approx \xi \left[1 - \frac{\xi \cdot \mathbf{x}}{\xi^2} - \frac{1}{2} \left(\frac{\xi \cdot \mathbf{x}}{\xi^2} \right)^2 - \dots \right] \quad (1.7)$$

Keeping only the linear term yields the Kirchhoff–Helmholtz transform

$$K_{KH}(\mathbf{r}) = -\frac{i}{2\lambda} \int_{\text{screen}} \left[\tilde{I}(\xi) \frac{1}{\xi^2} \left(1 + \frac{\xi}{L} \right) \right] \exp[-ik\xi \cdot \mathbf{x}/\xi] d\xi \quad (1.8)$$

Again, the function $K(\mathbf{r})$ is complex and significantly structured and different from 0 only in the space region occupied by the object. An algorithm has been developed for its evaluation that is outlined in the appendix, faster by many orders of magnitude than the direct evaluation of the double integral. Noteworthy is the fact that in this algorithm the pixel size in the reconstructed image can be chosen arbitrarily to achieve any magnification one wishes.

The complete procedure of DIHM is demonstrated in Fig. 1.3 and described in the figure caption. Noteworthy is the fact that reconstructing the hologram itself (i.e., without subtracting the background) leads to residual interference fringes and artificial features which are totally avoided if reconstruction is done from the contrast hologram. These fringes are, however, not due to the twin image as sometimes claimed in the literature without proof. Although in in-line holography with parallel light the twin image can be a problem, this is not the case in the point source geometry. The argument, substantiated with many experimental data reviewed here and presented elsewhere, is simple: the distance between source and object is typically hundreds or even thousands of wavelengths and the twin image is at the same distance on the other side of the source. The contribution of one on the other is an undetectable uniform background. The situation is vastly different, e.g., in photoelectron holography of surfaces, where source and object are angstroms apart, and the twin image is a problem although ways have been found to minimize its effect even in such unfavorable geometries.

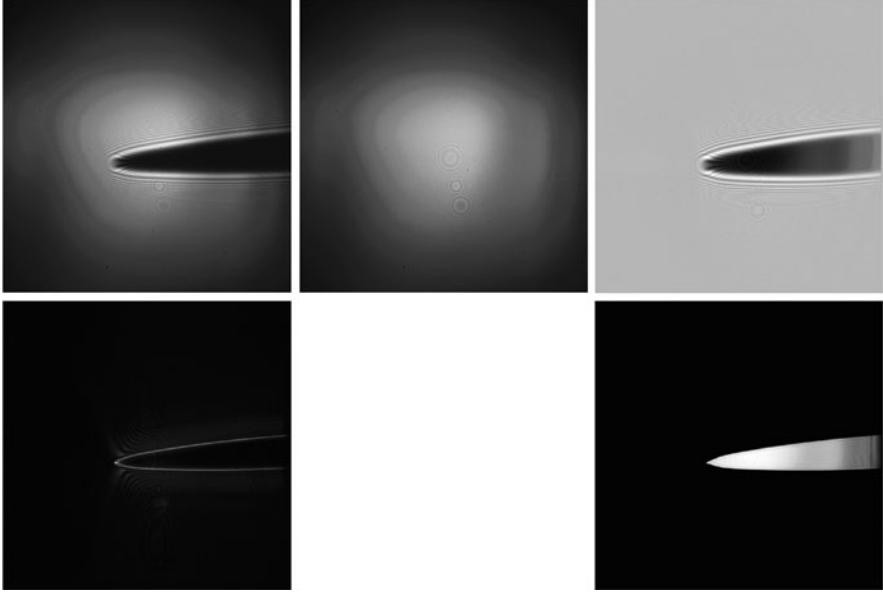


Fig. 1.3 Holography of a needle with blue light ($\lambda = 408$ nm), pinhole diameter $0.5 \mu\text{m}$, pinhole-object distance 1.1 mm, pinhole-CCD distance 20 mm, CCD chip size $1.28 \times 1.28 \text{ cm}^2$, $\text{NA} = 0.3$. *Top row*: hologram, background, and contrast hologram. *Bottom row, left*: reconstruction from original hologram and *right*: from contrast hologram. Reconstruction area $685 \times 685 \mu\text{m}$

1.4 Resolution and Depth of Field

We base our discussion of the lateral and depth resolution of DIHM on the point spread function psf. To obtain the psf we assume a perfect point source emitting a spherical wave $U_{\text{ref}}(\mathbf{r}) = U_0 r^{-1} \exp[ikr]$ with wavenumber $k = 2\pi/\lambda$. In addition we have a point object at a distance \mathbf{r}_1 along the optical axis from which scattered spherical waves emerge. The total wave field is thus

$$U(\mathbf{r}) = U_0 \frac{\exp[ikr]}{r} + U_1 \frac{\exp[ik|\mathbf{r} - \mathbf{r}_1|]}{|\mathbf{r} - \mathbf{r}_1|} \quad (1.9)$$

The intensity of the contrast image then becomes

$$\begin{aligned} \tilde{I}(\mathbf{r}) &= I(\mathbf{r}) - \frac{U_0^2}{r^2} \\ &= \frac{U_1^2}{|\mathbf{r} - \mathbf{r}_1|^2} + 2 \frac{U_0 U_1}{r |\mathbf{r} - \mathbf{r}_1|} \cos[k(r - |\mathbf{r} - \mathbf{r}_1|)] \end{aligned} \quad (1.10)$$

The first term accounts for classical scattering from an isolated object resulting in a smoothly varying background. The second term is due to interference between the

source and the object and represents holographic interference. Under holography conditions we must have $U_0 \gg U_1$. With the contrast intensity given on a screen with numerical aperture, NA, we can use the Kirchhoff–Helmholtz transform to calculate the reconstructed intensity around the original point source at \mathbf{r}_1 . This psf can be calculated analytically [19] and is given by

$$\text{psf}_{\text{NA}}(\mathbf{r}) = |K_{\text{NA}}(\mathbf{r})|^2 \quad (1.11)$$

$$K_{\text{NA}}(\mathbf{r}) = \sum_{n=0}^{\infty} \exp[ni\pi/2] a_n P_n \left(\frac{z - z_0}{|\mathbf{r} - \mathbf{r}_0|} \right) j_n(k |\mathbf{r} - \mathbf{r}_0|)$$

$$a_n = (n + 1/2) \int_{\sqrt{1-(\text{NA})^2}}^1 dt P_n(t) \quad (1.12)$$

The point spread function looks like a prolate spheroid with its long axis along the optical axis. In Fig. 1.4 we show views and cuts through the central point \mathbf{r}_1 in a plane perpendicular to the optical axis and along it. In holography it plays the role of the Debye integral in apertured optical systems. Similar arguments [27] result in estimates of the lateral and axial resolution

$$\delta_{\text{lat}} = \frac{\lambda}{2\text{NA}}$$

$$\delta_{\text{ax}} = \frac{\lambda}{2(\text{NA})^2}$$

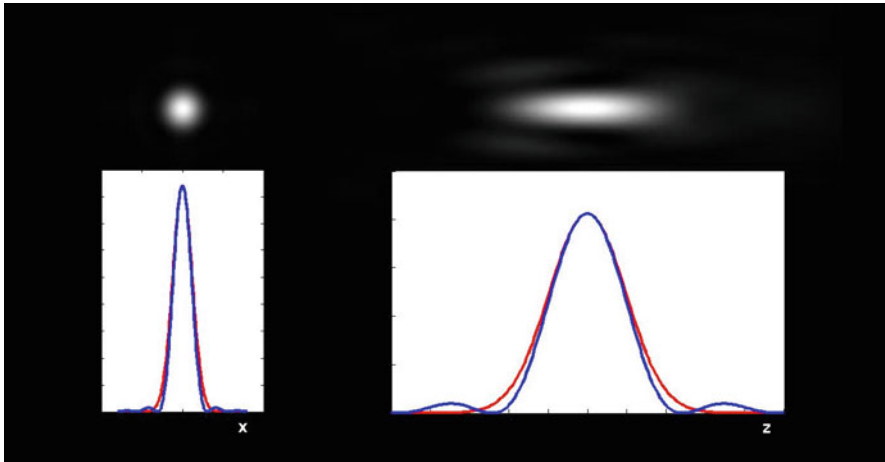


Fig. 1.4 Point spread function psf for NA=0.3. On the *left* (*right*) a view and cut perpendicular to (along) the optical axis

It is quite suggestive that a Gaussian

$$\text{psf}_{\text{NA}}(\mathbf{r}) \approx \frac{1}{2\pi\delta_{\text{lat}}^2} \exp\left[-(x^2 + y^2)/2\delta_{\text{lat}}^2\right] \frac{1}{\delta_{\text{ax}}\sqrt{2\pi}} \exp\left[-z^2/2\delta_{\text{ax}}^2\right] \quad (1.13)$$

represents an acceptable approximation for psf_{NA} .

For a perfect pinhole the numerical aperture of DIHM depends on the ratio of the detector width to the object – detector distance. The resolution thus increases at shorter wavelength and with larger screen width (larger NA). When the optical path crosses several media with different refractive indexes, hologram formation depends on an effective wavelength that is determined by the length of path through each medium as we will discuss below in connection with immersion holography.

The resolution of a holographic microscope can also be discussed in terms of the number of interference fringes that can be resolved by the recording medium [28, 30]. In the case of digital CCD or CMOS detectors, faithful recording of interference fringes is only possible if the pixel size of the recording chip is much smaller than the smallest fringe spacing that needs to be recorded. Simulations with computer-generated holograms suggested that two scattering centers can be resolved if the number of captured fringes is large (tens of fringes) and that only fringes separated by more than three camera pixels contribute to image reconstruction and resolution. Either too few fringes or fringes that are too close together will lead to reduced resolution. In general, a shorter wavelength will produce more fringes, and usually results in higher resolution. However, the larger number of fringes is spread over a fixed number of pixels on the chip so that at shorter wavelength the average number of pixels per fringe decreases and the resolution may thus be less than expected. A more detailed discussion on fringe number and spacing and its effect on resolution can be found elsewhere [29, 30].

Point source DIHM with a nearly spherical reference wave produces a magnified hologram at the recording screen. This implies that the number of fringes captured, and hence the resolution, depends on the object–screen distance as well. A resolution of 1 μm is easily obtainable with the object close to the point source and the smallest measurable separation of two scattering points increases nearly linearly with source – object distance. The imaged volume is essentially determined by the volume of a pyramid that has the CCD chip as a base and the point source as the apex.

One of the most amazing advantages of holographic microscopy, and in particular of pointsource DIHM, is the fact that a single 2-D hologram produces in reconstruction a 3-D image of the object without loss of resolution. This is in sharp contrast to compound microscopy where the depth of field reduces sharply with improving resolution necessitating refocussing to map out a larger volume. To show this advantage we have embedded 1 μm latex beads in gelatin on a cover slide (to immobilize them), taken one hologram and made five reconstructions at different depths from 300 μm to 3 mm from the cover slide, see Fig. 1.5.

Lastly, we investigate the effect of the pinhole size. In Fig. 1.6 panel A shows the hologram and panels B and C reconstructions at 3 and 2 mm, respectively, with

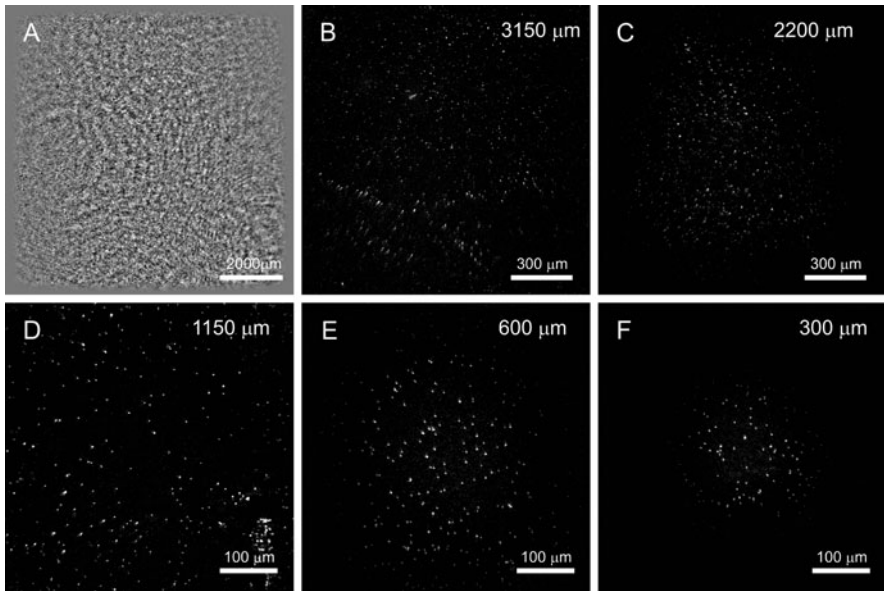


Fig. 1.5 Depth of field: $1\text{ }\mu\text{m}$ latex beads embedded in gelatin on a cover slide (to immobilize them). (a) hologram taken with blue light. (b–f) five reconstructions at different depths from $300\text{ }\mu\text{m}$ to 3 mm from the cover slide

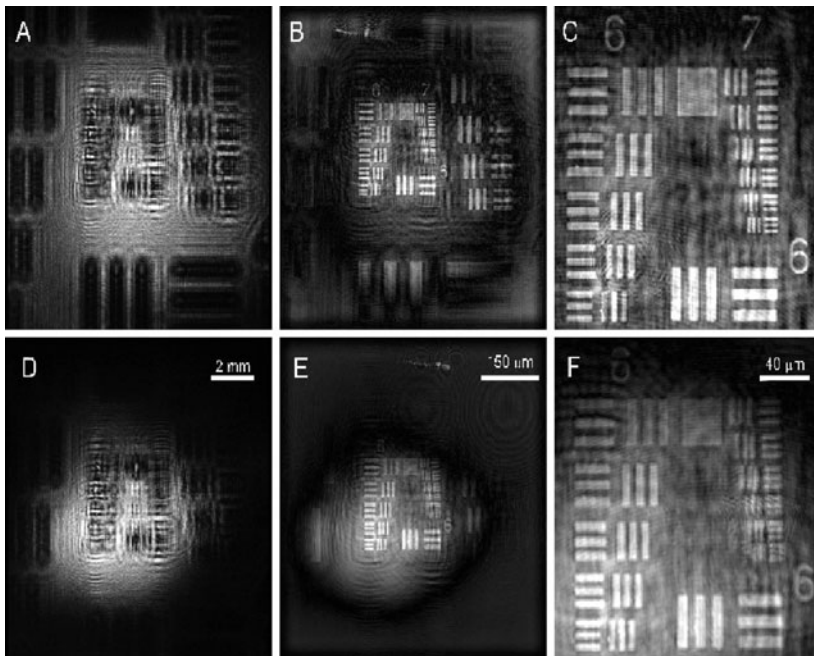


Fig. 1.6 Pinhole size effect: (a) Hologram with $0.5\text{ }\mu\text{m}$ pinhole, (b) reconstruction, and (c) central section of reconstruction only. (d–f) same for $2\text{ }\mu\text{m}$ pinhole. Laser wavelength 408 nm and numerical aperture $\text{NA} = 0.208$

a field of view of 1.4 mm. The pinhole was $0.5\ \mu\text{m}$ in diameter and the numerical aperture was 0.2. For panels D to F the pinhole was increased to $2\ \mu\text{m}$ thus reducing the numerical aperture so much that the outline of the finite emission cone is seen.

1.5 Deconvolution

As in any optical instrument, resolution and image quality are dictated by the instrument function. In DIHM, limiting factors are the finite extent of the point source and the numerical aperture. For both of these effects it is easy to calculate the point spread function psf given in (1.11) in the previous section. We thus have for the image obtained at finite NA

$$I_{\text{NA}}(\mathbf{r}) = \int d\mathbf{r}' \text{psf}_{\text{NA}}(\mathbf{r} - \mathbf{r}') I(\mathbf{r}') \quad (1.14)$$

where $I(\mathbf{r}')$ is the “perfect” image at $\text{NA}=1$. Taking Fourier transforms we have

$$\mathcal{F}(I_{\text{NA}}) = \mathcal{F}(\text{psf})\mathcal{F}(I) \quad (1.15)$$

and an inverse Fourier transform yields the deconvoluted “perfect” image

$$I = \mathcal{F}^{-1}[\mathcal{F}(I_{\text{NA}})/\mathcal{F}(\text{psf})] \quad (1.16)$$

Note that for the parametrization (1.13) of the psf its Fourier transform is again a product of Gaussians.

An application of the deconvolution procedure is given in Fig. 1.7 for $\text{NA}=0.3$ showing clusters of $1\ \mu\text{m}$ latex beads which after deconvolution are clearly identified.

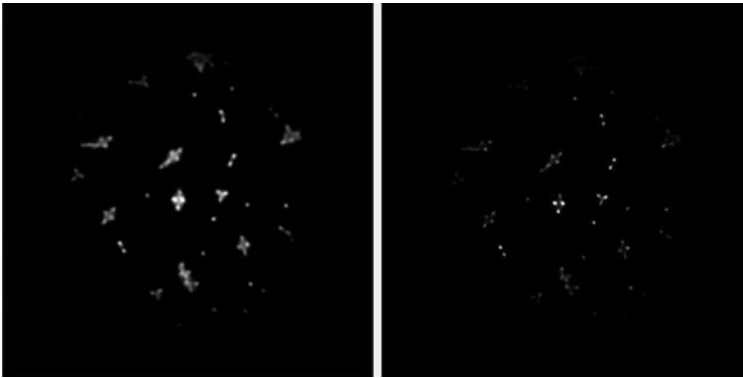


Fig. 1.7 Cluster of $1\ \mu\text{m}$ latex beads. On the *left* taken with numerical aperture $\text{NA}=0.3$. On the *right* after deconvolution

1.6 Immersion Holography

To improve the resolution of DIHM one has two obvious options, as with any type of microscopy:

1. Reduce the wavelength, say into the ultraviolet regime. This produces three challenges: (a) UV lasers are expensive, large and more elaborate, and dangerous; (b) one needs a pinhole with a diameter of a few hundred nanometers; they are expensive, difficult to make, and easily clog up; and (c) one needs a camera sensitive to UV radiation, again an expensive undertaking.
2. Increase the numerical aperture requiring a larger camera chip at more expense.

An elegant solution to this challenge is much akin to the use of oil immersion lenses in compound microscopy. One realizes that the hologram is formed when the scattered wave interferes with the reference wave. This happens in the space region between the object and the detector. If one therefore fills this region with a material of high refractive index n then the hologram is formed at a wavelength λ/n , or, alternatively, with a numerical aperture enlarged by a factor n , see Fig. 1.8. Thus for experiments on biological species in water a blue laser ($\lambda = 408 \text{ nm}$) is sufficient to do DIHM in the UV range at 308 nm increasing the resolution by 30%. Or using oil ($n = 1.5$) or sapphire glass ($n = 1.8$) we would work at $\lambda/n = 272$ and 227 nm , respectively. If the space between the object and the CCD chip is not completely filled with the high index of refraction material, geometric optics leads to an effective wavelength

$$\lambda_{\text{eff}} = \lambda / [(L - H) + nH] / L \quad (1.17)$$

An example of immersion holography is shown in Fig. 1.9, again for clusters of latex beads.

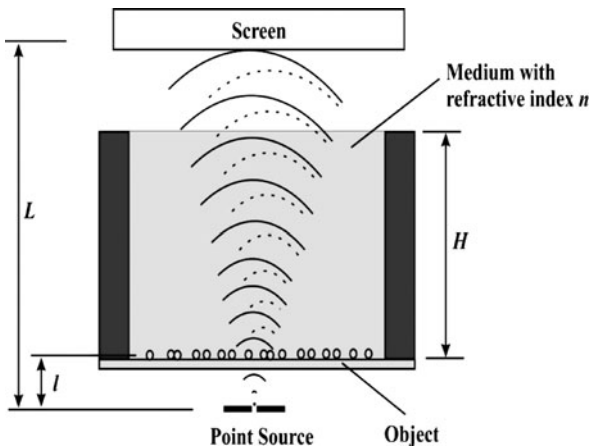


Fig. 1.8 Schematic for immersion holography [32]

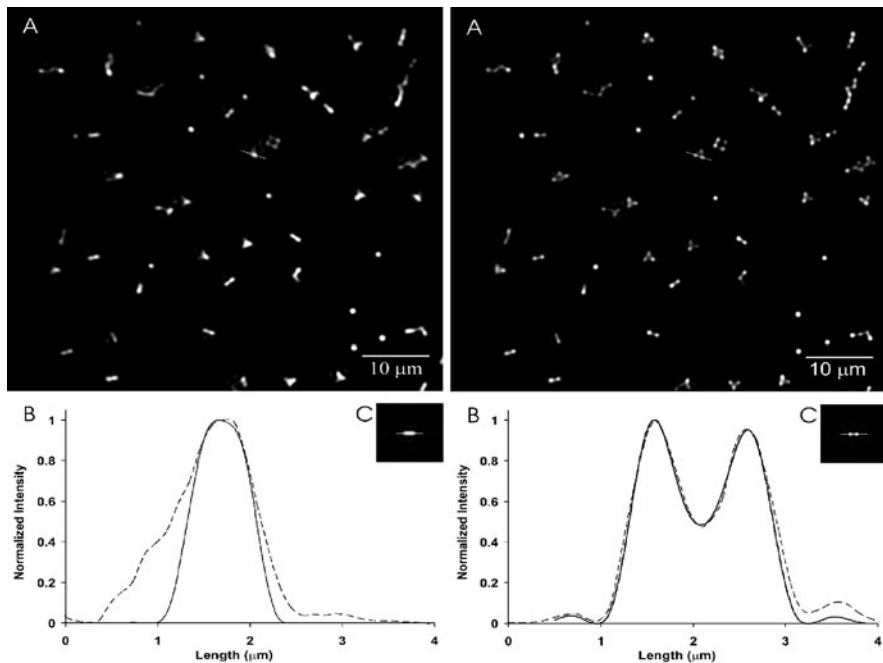


Fig. 1.9 (a) Reconstruction of a deposit of 1.09 μm beads on a cover slide showing single beads and small clusters. (b) Intensity profile through a dimer. *Left*: with green light and air between cover slide and CCD chip. *Right*: with space filled with oil of $n = 1.5$ [32]

1.7 Phase images

The Kirchhoff–Helmholtz transform yields the wave front at the object with both amplitude and phase information. There are occasionally claims in the literature that point source DIHM is of limited value because it is not capable of producing phase images. These arguments are hard to follow and will not be repeated here. Instead we present an example that shows clearly the capability and superiority of point source DIHM. The task at hand was to map the index of refraction across the core of a fiber optic cable where it is enhanced by about a percent over the value in the glass cladding by doping with rare earth materials. Because the cladding will act as a cylindrical lens one must immerse the fiber into oil with matching refractive index. Panel A of Fig. 1.10 shows the hologram taken with a violet laser ($\lambda = 405$ nm), panel B shows the reconstructed intensity, and panel C the reconstructed phase. One can still see the remnants of the cladding because the oil was not matching the refractive index of the cladding perfectly. Cuts perpendicular to the core showing intensity (panel E) and phase (panel F) confirm that the core is 4.5 μm in diameter as stated by the manufacturer. Assuming that the core is cylindrical we can calculate the optical path length in the core to be $p(r) = 2(R^2 - r^2)^{1/2}$ where R is the radius

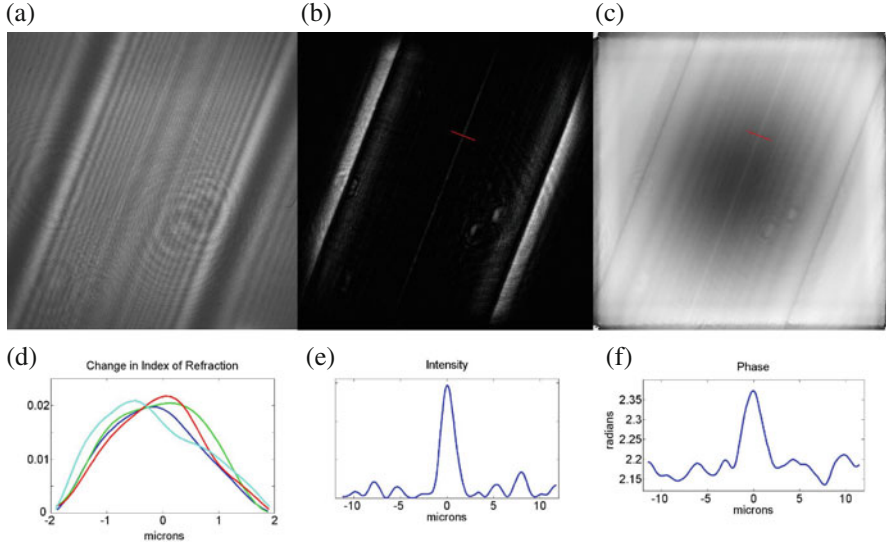


Fig. 1.10 Optical fiber immersed in oil with matching refractive index. *Panel A* shows the hologram taken with a blue laser, *panel B* the reconstructed intensity, and *panel C* the reconstructed phase. Cuts perpendicular to the core showing intensity (*panel E*) and phase (*panel F*) confirm that the core is $4.5\ \mu\text{m}$ in diameter. *Panel D* profiles in the index of refraction at four different positions along the core

of the core and r is the lateral distance from its center. Thus we get for the phase difference with respect to the cladding

$$\Delta\phi(r) = p(r)\Delta n(r) \quad (1.18)$$

where $\Delta n(r)$ is the change of the refractive index of refraction throughout the core which is obtained from $\Delta\phi$ by a simple division. The resulting profiles in the index of refraction at four different positions along the core (Panel D) confirm that the core was tapered with the maximum enhancement of the refraction index about 0.02 with a considerable inhomogeneity along the core and across it.

1.8 4-D Imaging

In many fields of science and technology the microscopist is faced with tracking many objects such as particulates, bubbles, plankton, or bacteria as they move in space, asking for an efficient way of 4-D particle tracking. DIHM is the perfect tool to do this job [31, 32]: 4-D tracking is achieved by (1) recording digitally, e.g., on a CCD chip, a film of N holograms h_1, h_2, h_3, \dots at times t_1, t_2, t_3, \dots (2) One constructs digitally a difference hologram $(h_1 - h_2) + (h_3 - h_4) + (h_5 - h_6) + \dots$, thus retaining only those features in the holograms that correspond to moving objects;

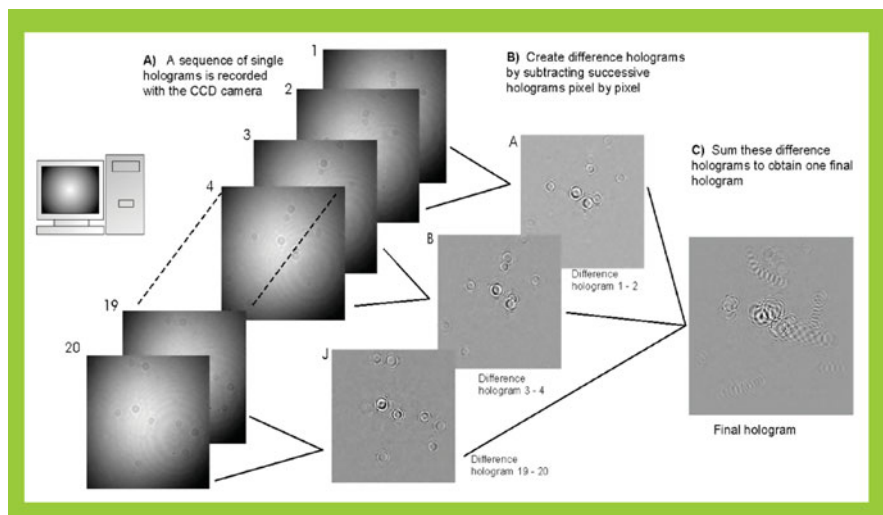


Fig. 1.11 Procedure to obtain the 3-D structures of moving objects from a sequence of holograms by subtracting subsequent holograms, then adding these difference holograms into a final compound hologram from which reconstructed trajectories are obtained with the Helmholtz–Kirchhoff transform

the recording speed must be adjusted accordingly. Because holography is linear in the scattering amplitude the superposition principle holds and adding or subtracting holograms does not lead to a loss of information. By subtracting two holograms and then adding the differences one ensures that (a) the pixels do not saturate and (b) one at least partially reduces the noise in the original holograms. This construct also reduces the size of the data set by a factor of N . Data from different experiments with hundreds of holograms done at different times can be “added” this way for storage. (3) Lastly, one numerically reconstructs a stack of images in a sufficient number of planes throughout the sample volume so that a 3-D rendering displays the tracks of all the moving particles. A schematic of this procedure is shown in Fig. 1.11. One could also reconstruct stacks of images from each frame in the film of holograms and would then be able to produce a 3-D movie of the motion itself.

1.9 Applications in Microfluidics

As an application of 4D tracking of micron-sized objects [33–37] we show in Fig. 1.12 the trajectories of latex beads of $1\ \mu\text{m}$ diameter suspended in water flowing around a $70\ \mu\text{m}$ large bead. The time between successive exposures is $1/15\ \text{s}$. Because we also can measure the distance traveled between exposures we can evaluate the velocity vector field in 3-D.

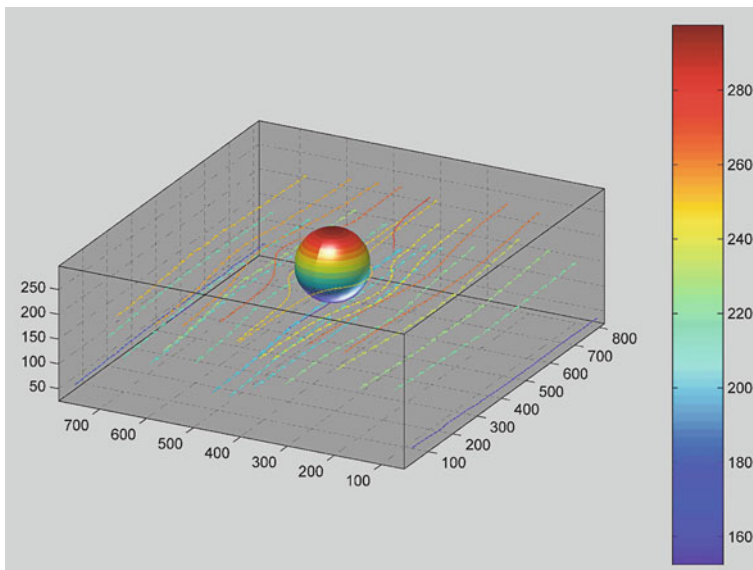


Fig. 1.12 Trajectories of $1\ \mu\text{m}$ latex beads suspended in water flowing around a $70\ \mu\text{m}$ large bead. The time between successive exposures is $1/15\ \text{s}$

1.10 Biology

We show a few examples of imaging biological species with DIHM [38–40] starting in Fig. 1.13 with a high-resolution image of a diatom.

Our next example is an image of *Escherichia coli* bacteria, see Fig. 1.14.

To demonstrate that DIHM is also capable of imaging large objects with micron detail we show in Fig. 1.15 a section through the head of a fruitfly, *Drosophila melanogaster*. Such images reveal the structure of the pigmented compound eye,

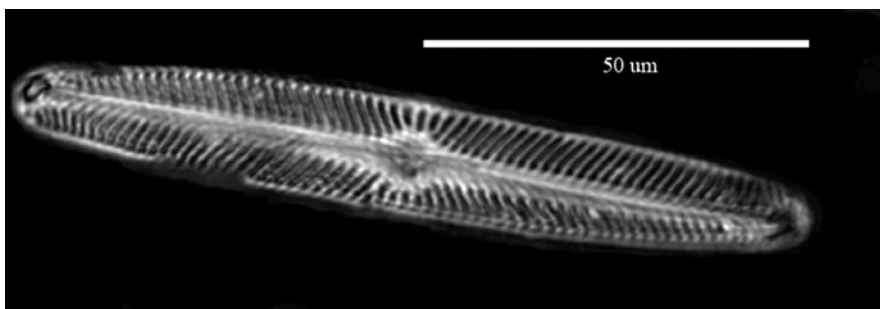


Fig. 1.13 High-resolution reconstruction of a diatom. The hologram was taken with a blue laser at $\lambda = 408\ \text{nm}$



Fig. 1.14 *E.coli* bacteria imaged with a blue laser. Pinhole–object distance 300 μm , pinhole–screen distance 15 mm, pinhole 0.5 μm . Bacteria diameter about 1 μm

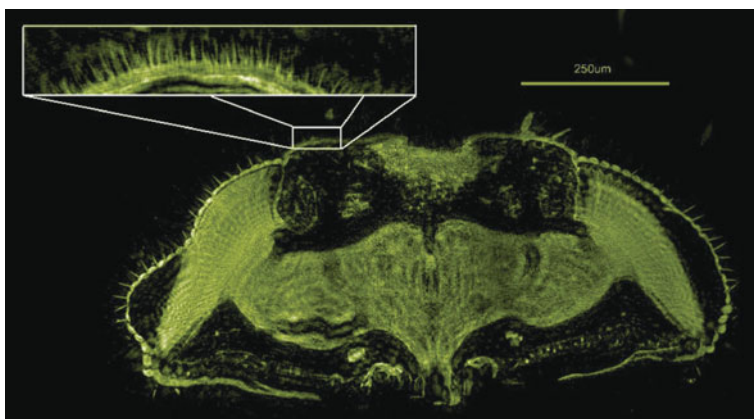


Fig. 1.15 A section through the head of a fruitfly with a blue laser at $\lambda = 408 \text{ nm}$

and different neuropile regions of the brain within the head cuticle including the optic neuropiles underlying the compound eye.

Our last example in biology is a 3-D rendering of a suspension of *E. coli* bacteria in a stream of growth medium around a big sphere, see Fig. 1.16. Experiments like these allow, for the first time, realistic studies of the colonization of surfaces by bacteria and the mechanism of biofilm formation.

DIHM was also used in a large study of the effect of temperature on motility of three species of the marine dinoflagellate *Alexandrium* which made full use of the 3-D trajectories to extract quantitative information on their swimming dynamics [39, 40].

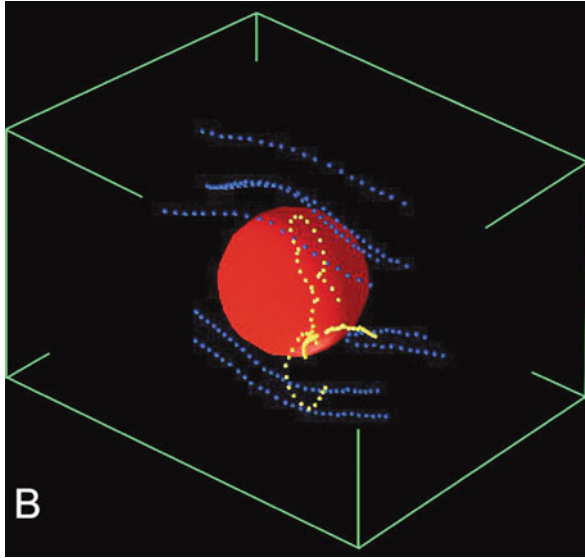


Fig. 1.16 3-D rendering of the tracks of a suspension of *E. coli* bacteria in a stream of growth medium around a big sphere. Holography with blue light ($\lambda = 408$ nm), pinhole diameter $0.5\ \mu\text{m}$, pinhole–object distance 0.5 mm, pinhole–CCD distance 19 mm, CCD chip size $1.28 \times 1.28\ \text{cm}^2$, NA = 0.3 . Reconstruction volume $300 \times 300 \times 300\ \mu\text{m}^3$. Recording the motion at 15 f/s

1.11 Submersible DIHM

To allow observations with DIHM in ocean or lake environments we have constructed an underwater microscope. Its schematic is shown in Fig. 1.17: The microscope consists of two pressure chambers one of which contains the laser and the other the CCD camera (plus power supply). The two chambers are kept at a fixed distance to each other to allow water to freely circulate between them. In the center of the chamber plates facing each other are small windows with the one on the laser chamber having the pinhole. The signal from the CCD camera is transmitted via an underwater USB cable to a buoy or a boat above from where a satellite link can be established for data transmission to a laboratory. Depending on the design of the pressure chamber water depths of several hundred meters are easily accessible and can be extended to thousands of meters with high pressure technology. The prototype was pressure tested to 10 atm and operated at 20 m depth and has given the same performance as far as resolution is concerned as the desktop version of DIHM.

Fig. 1.18 shows a Rotifer (length $200\ \mu\text{m}$, width $100\ \mu\text{m}$) swimming at a speed of 2.5 mm/s at a depth of 15 m in the North Atlantic.

As a last example we show in Fig. 1.19 the tracks of algae in permafrost springs on Axel Heiberg Island in the High Arctic. A light weight underwater DIHM was used in this expedition.

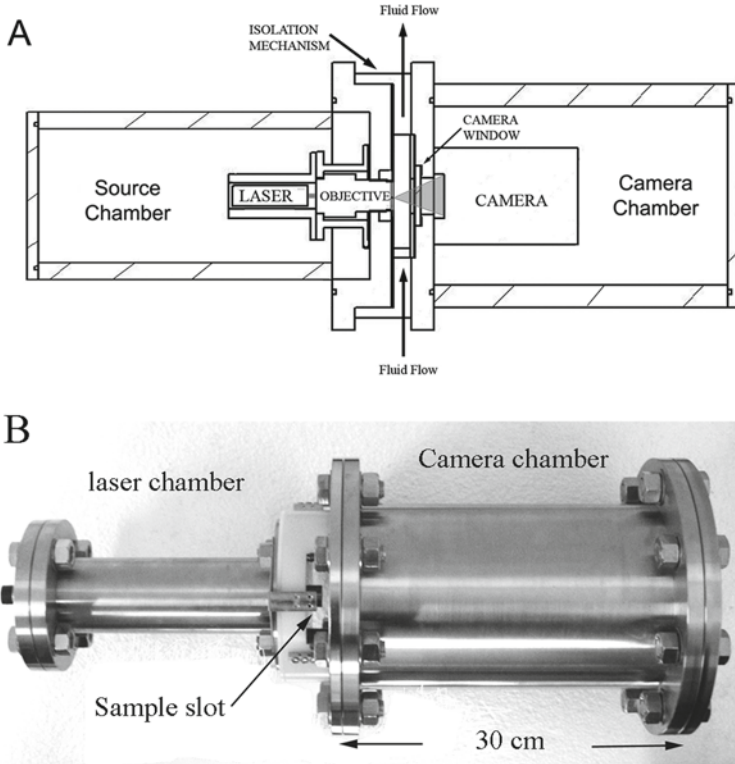


Fig. 1.17 Drawing and instrument of the underwater DIHM microscope, courtesy of Resolution OpticsInc, Halifax NS [30]

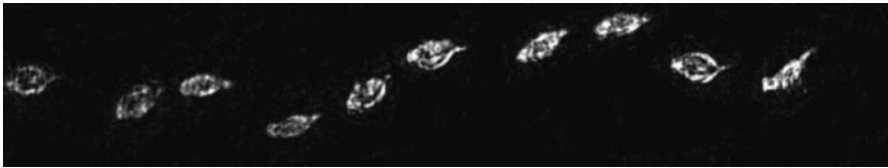


Fig. 1.18 Rotifer (length $200\ \mu\text{m}$, width $100\ \mu\text{m}$) swimming at a speed of $2.5\ \text{mm/s}$. Remote observation at a depth of $15\ \text{m}$ in the North Atlantic [30]

1.12 Recent progress

In this chapter we want to highlight some recent advances in point source DIHM. We begin with the work by Repetto et al. [41] on lensless digital holographic microscopy with light-emitting diode illumination in which they show that the spatial coherence of light emitting diodes is good enough to obtain resolution of a few microns. Due to the low intensity of LEDs the pinhole has to be rather large (about $5\ \mu\text{m}$) to get enough illumination. With the advent of more powerful LEDs this opens up a very cheap approach to DIHM [42–44].

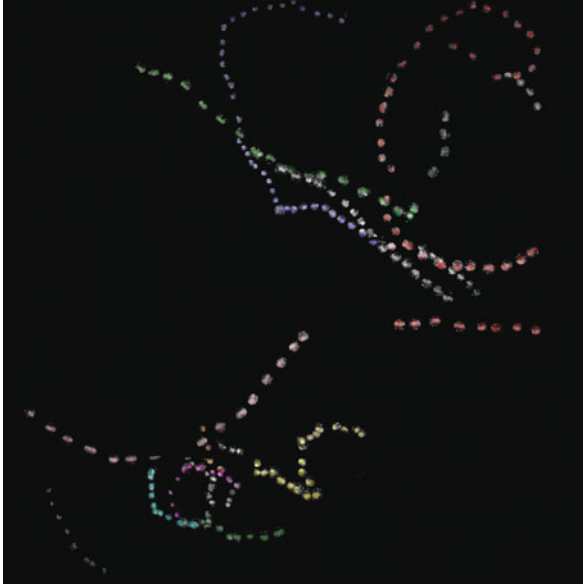


Fig. 1.19 Algae in permafrost springs on Axel Heiberg Island. Holography with blue light ($\lambda = 408$ nm), pinhole diameter $0.5\text{ }\mu\text{m}$, pinhole–object distance 0.8 mm, pinhole–CCD distance 21 mm, CCD chip size $1.28 \times 1.28\text{ cm}^2$, $\text{NA} = 0.3$. Reconstruction volume $500 \times 500 \times 300\text{ }\mu\text{m}^3$, framerate 15 f/s [58]

As methods are devised for larger numerical apertures new techniques for rapid reconstruction are also called for. A first step in this direction uses a reorganized hologram with a low number of pixels, the tile superposition technique [45, 46]. The algorithm was applied to imaging of a $2\text{ }\mu\text{m}$ bead cluster and was shown to be superior. It was argued in these papers that this could become the base for high-resolution wide-field imaging by multispot illumination [47–49]. Another new approach advancing a method of multiplane interference and diffraction detection also looks very promising [50–52].

Underwater DIHM has been used for an extensive European study of biofouling phenomena in the marine environment, called AMBIO – Advanced Nanostructured Surfaces for the Control of Biofouling – (<http://www.ambio.bham.ac.uk>). In the papers by Heydt et al. [53, 54] new ways to cope with a mass of data on moving algae and bacteria have been developed and these observations were combined in general systems approach with surface and polymer chemistry to identify preventative measures to control biofouling [55].

1.13 Summary and Discussion

We want to conclude underlining some remarkable characteristics of DIHM and the underwater DIHM:

1. Simplicity of the microscope: DIHM, as well as underwater DIHM, is microscopy without objective lenses. The hardware required for the desktop version is a laser, a pinhole, and a CCD camera. For the underwater DIHM version we need the same elements contained in submersible hermetic shells.
2. Maximum information: A single hologram contains all the information about the 3-D structure of the object. A set of multiple holograms can be properly added to provide information about 4-D trajectories of samples.
3. Maximum resolution: Optimal resolution, of the order of the wavelength of the laser, can be obtained easily with both versions.
4. Simplicity of sample preparation, particularly for biological samples where no sectioning or staining are required, so that living cells and specimens can be viewed. Indeed, for the underwater DIHM there is no sample preparation at all, and real-time information of living organism can be retrieved remotely.
5. Speed: The kinetics of the sample, such as particle motion or metabolic changes in a biological specimen, can ultimately be followed at the capture rate of the image acquisition system.
6. 4-D tracking: A large number of particles can be tracked simultaneously in 3-D as a function of time.

Regarding the 4-D tracking, feasible in both versions of the DIHM, we emphasize the efficiency in data collection in our procedure. Removal of background effects and construction of summed holograms are easily accomplished so that high-resolution tracking of many particles in 4-D can be obtained from just one difference hologram. Since resolutions on the order of the wavelength of light have been achieved with DIHM, tracking of organisms as small as bacteria is possible, as would the motion of plankton in water or, at lower resolution, the aerial trajectories of flying insects. DIHM can also be used successfully on macroscopic biological specimens, prepared by standard histological procedures, as for a histological section of the head of the fruit fly.

Outside of biology, applications of 4-D DIHM have been demonstrated in microfluidics for particle velocimetry, i.e., tracking of the motion of particles in liquid or gas flows, gas evolution in electrolysis, and in the visualization of structures in convective or turbulent flow. Further applications have dealt with colloidal suspensions, remote sensing and environmental monitoring, investigation of bacterial attachment to surfaces and biofilm formation, and many more. DIHM with its inherent ability to obtain magnified images of objects (unlike conventional off-axis holography) is therefore a powerful new tool for a large range of research fields. Films on 4-D tracking and more examples can be viewed at <http://www.physics.dal.ca/~kreuzer> and in the supplementary material of this chapter. The results from the expedition to Axel Heiberg island have now been published [58].

This work was supported through grants from the Natural Sciences and Research Council of Canada and the Office of Naval Research, Washington.

Appendix: Kirchhoff–Helmholtz Reconstruction Algorithm

Introduction

The role of reconstruction in holography is to obtain the 3-D structure of the object from the 2-D hologram on the screen, or, in technical terms, to reconstruct the wave front at the object. This can be achieved via a Kirchhoff–Helmholtz transform

$$K(\mathbf{r}) = \int_S d^2\xi I(\xi) \exp(ik\xi \cdot \mathbf{r}/\xi) \quad (1.19)$$

where the integration extends over the 2-D surface of the screen with coordinates $\xi = (X, Y, L)$ where L is the distance from the source to the (center of the) screen. $k = 2\pi/\lambda$ is the wave number of the radiation (electromagnetic, acoustic, electrons, or matter) and $I(\xi)$ is the contrast image (hologram) on the screen obtained by subtracting the images with and without the object present. The function $K(\mathbf{r})$ is significantly structured and different from 0 only in the space region occupied by the object. By reconstructing the wave front $K(\mathbf{r})$ on a number of planes at various distances from the source in the vicinity of the object, a 3-D image can be built up from a single 2-D hologram. $K(\mathbf{r})$ is a complex function and one usually plots its magnitude to represent the object, although phase information can also be extracted.

The Kirchhoff–Helmholtz transform is sometimes given in polar coordinates

$$\begin{aligned} \hat{k}_x &= X/\sqrt{X^2 + Y^2 + L^2} \\ \hat{k}_y &= Y/\sqrt{X^2 + Y^2 + L^2} \end{aligned} \quad (1.20)$$

for which (1.1) reads

$$K(\mathbf{r}) = \int_S I(\hat{k}_x, \hat{k}_y) \exp(ikz\sqrt{1 - \hat{k}_x^2 - \hat{k}_y^2}) \exp(ik(x\hat{k}_x - y\hat{k}_y)) J(\hat{k}_x, \hat{k}_y) d\hat{k}_x d\hat{k}_y \quad (1.21)$$

where the Jacobian is given by

$$J(\hat{k}_x, \hat{k}_y) = L^2/(1 - \hat{k}_x^2 - \hat{k}_y^2)^4 \quad (1.22)$$

We should point out that setting this Jacobian equal to 1, which, in some measure, amounts to using an on-axis approximation in half of the integrand, is so crude an approximation that optimal resolution cannot be achieved. Unfortunately it is invoked by several groups but should be avoided at all cost.

The numerical implementation of the full Kirchhoff–Helmholtz transform is very time consuming, even on the fastest computers, because the nonlinear phase factor in the exponential function prohibits the straightforward application of fast Fourier transform (FFT) methods. Our solution of the problem, which is at least a factor

of 10^3 faster than the direct evaluation and thus makes numerical reconstruction practical, consists of five steps [56]:

1. A coordinate transformation to cast the Kirchhoff–Helmholtz transform into a standard 2-D Fourier transform.
2. Discretization of the double integral into a double sum.
3. Interpolation of the hologram on an equidistant point grid.
4. Re-writing the Kirchhoff–Helmholtz transform as a convolution.
5. Application of three FFTs to get the result.

This solution was first conceived on March 16, 1992 while at the APS meeting in Indianapolis and was implemented and running within a week.

Coordinate Transformation

To eliminate the nonlinearity in the phase factor we perform a coordinate transformation

$$\begin{aligned} X' &= XL/R \\ Y' &= YL/R \\ R &= (L^2 + X^2 + Y^2)^{1/2} \end{aligned} \quad (1.23)$$

with the inverse transformation

$$\begin{aligned} X &= X'L/R' \\ Y &= Y'L/R' \\ R' &= L^2/R = (L^2 - X'^2 - Y'^2)^{1/2} \end{aligned} \quad (1.24)$$

and the Jacobian

$$dXdY = (L/R')^4 dX'dY' \quad (1.25)$$

This results in

$$K(\mathbf{r}) = \int_{S'} dX'dY' I'(X', Y') \exp[ik(xX' + yY')/L] \quad (1.26)$$

with

$$I'(X', Y') = I(X(X', Y'), Y(X', Y'))(L/R')^4 \exp(ikzR'/L) \quad (1.27)$$

Note that if the screen S is rectangular then S' becomes barrel shaped with more rounding of the edges for a larger ratio of screen width to L.

Discretization

To evaluate (1.8) with FFT techniques we must rewrite it in discrete form as

$$K_{nm} = \sum_{j,j'=0}^{N-1} I'_{jj'} e^{2\pi i(nj+mj')/N} \quad (1.28)$$

where N , the number of pixels in one direction of the screen, will be arranged to be a multiple of 2. For simplicity we restrict the following presentation to the situation where a quadratic screen is used. We therefore write

$$\begin{aligned} x &= x_n = x_0 + n\delta_x \\ y &= y_n = y_0 + n\delta_y \end{aligned} \quad (1.29)$$

for $n, m = 0, 1, 2, \dots, N - 1$. Likewise we write

$$\begin{aligned} X' &= X'_j = X'_0 + j\Delta'_x \\ Y' &= Y'_j = Y'_0 + j'\Delta'_y \end{aligned} \quad (1.30)$$

for $j, j' = 0, 1, 2, \dots, N - 1$.

Interpolation

Experimental holograms are usually recorded on a flat screen, perpendicular to the optical axis, and digitized on an equidistant grid of pixels

$$\begin{aligned} X &= X_j = X_0 + j\Delta_x \\ Y &= Y_j = Y_0 + j'\Delta_y \end{aligned} \quad (1.31)$$

which, under the transformation (1.5), are transformed into non-equidistant points (X'_j, Y'_j) , the set of these points is S' .

We therefore construct a rectangular screen S'' that circumscribes S' , and introduce a new set of equidistant points (1.12) where

$$\begin{aligned} X'_0 &= X_0 L / \sqrt{L^2 + X_0^2} \\ Y'_0 &= Y_0 L / \sqrt{L^2 + Y_0^2} \\ \Delta'_x &= \frac{L[(X_0 + (N-1)\Delta_x)]}{N\sqrt{L^2 + [(X_0 + (N-1)\Delta_x]^2}} - \frac{LX_0}{N\sqrt{L^2 + X_0^2}} \\ \Delta'_y &= \frac{L[(Y_0 + (N-1)\Delta_y)]}{N\sqrt{L^2 + [(Y_0 + (N-1)\Delta_y]^2}} - \frac{LY_0}{N\sqrt{L^2 + Y_0^2}} \end{aligned} \quad (1.32)$$

With this we get the Kirchhoff–Helmholtz transform (1.1) into the discrete form

$$K_{nm} = \Delta'_x \Delta'_y \exp \{ ik [(x_0 + n\delta_x)X'_0 + (y_0 + m\delta_y)Y'_0] / L \} \\ \times \sum_{j,j'=0}^{N-1} I'_{jj'} \exp \left[ik(jx_0\Delta'_x + j'y_0\Delta'_y)/L \right] \exp \left[ik(nj\delta_x\Delta'_x + mj'\delta_y\Delta'_y)/L \right] \quad (1.33)$$

where $I'_{jj'}$ is the image interpolated at the points (1.12). This can be cast into a form suitable for FFT techniques if we choose

$$\delta_x = \frac{\lambda L}{N\Delta'_x} \\ \delta_y = \frac{\lambda L}{N\Delta'_y} \quad (1.34)$$

where $\lambda = 2\pi/k$ is the wavelength of the illuminating radiation. We point out that situating the screen symmetrically about the optical axis simplifies all of the above formulae considerably.

Convolution

The advantage of using FFT techniques is obviously their speed, i.e., one gains a factor 10^3 over a direct evaluation of (1.1). The disadvantage, however, is the fact that (1.16) imposes the resolution of the reconstruction. We overcome this limitation by rewriting (1.15) as a convolution and then use the product theorem of Fourier transforms.

We write

$$nj = [n^2 + j^2 - (n - j)^2] / 2 \quad (1.35)$$

and get

$$K_{nm} = \Delta'_x \Delta'_y \exp \{ ik [(x_0 + n\delta_x)X'_0 + (y_0 + m\delta_y)Y'_0] / L \} \\ \times \exp \left\{ ik(n^2\delta_x\Delta'_x + m^2\delta_y\Delta'_y)/2L \right\} \quad (1.36)$$

$$\times \sum_{j,j'=0}^{N-1} I'_{jj'} \exp \left[ik(jx_0\Delta'_x + j'y_0\Delta'_y + j^2\delta_x\Delta'_x/2 + j'^2\delta_y\Delta'_y/2)/L \right] \\ \times \exp \left[-ik((n - j)^2\delta_x\Delta'_x + (m - j')^2\delta_y\Delta'_y)/2L \right] \quad (1.37)$$

Let us then take the following FFTs:

$$K'_{vv'} = \sum_{j,j'=0}^{N-1} I'_{jj'} \exp \left[ik(jx_0\Delta'_x + j'y_0\Delta'_y + j^2\delta_x\Delta'_x/2 + j'^2\delta_y\Delta'_y/2)/L \right] \\ \times \exp[2\pi i(vj + v'j')/N] \quad (1.38)$$

$$R_v = \sum_{j=0}^{N-1} \exp\{-ikj^2\delta_x\Delta'_x/2L\} \exp[2\pi ivj/N] \quad (1.39)$$

An inverse FFT then yields

$$K_{nm} = \Delta'_x\Delta'_y \exp \left\{ ik \left[(x_0 + n\delta_x)X'_0 + (y_0 + m\delta_y)Y'_0 \right] / L \right\} \\ \times \exp \left\{ ik(n^2\delta_x\Delta'_x + m^2\delta_y\Delta'_y)/2L \right\} \quad (1.40)$$

$$\times \sum_{v,v'} K'_{vv'} R_v R_{v'} \exp\{-2\pi i(vn + v'm)/N\} \quad (1.41)$$

In the numerical implementation care must be exercised in treating end effects by zero padding.

The generalization of the method to nonsymmetric screens and to reconstruction on planes arbitrarily tilted with respect to the optical axis has also been implemented.

For the numerical implementation of the transform, we have developed a very fast algorithm incorporated in a self-contained programme package called DIHM [57] that not only does the numerical reconstruction but also all other procedures connected with data management and visualization.

References

1. D. Gabor, A new microscopic principle. *Nature (London)* **161**, 777–778 (1948)
2. E.N. Leith, J. Upatnieks, Reconstructed wavefronts and communication theory. *J. Opt. Soc. Am.* **52**, 1123 (1962); *ibid.* **53**, 1377 (1963); *ibid.* **54**, 1295 (1963)
3. J.W. Goodman, R.W. Lawrence, Digital image formation from electronically detected holograms. *Appl. Phys. Lett.* **11**, 77–79 (1967)
4. P. Hariharan, *Optical Holography* (Cambridge University Press, Cambridge, 1996)
5. T. Kreis, *Holographic Interferometry* (Akademie Verlag, Berlin, 1996)
6. D. Gabor, Microscopy by reconstructed wavefronts. *Proc. R. Soc. London, Ser. A* **197**, 454 (1949)
7. Y. Aoki, Optical and numerical reconstruction of images from sound-wave holograms. *IEEE Trans. Acoust. Speech AU-18*, **258** (1970)
8. M.A. Kronrod, L.P. Yaroslavski, N.S. Merzlyakov, Computer synthesis of transparency holograms. *Sov. Phys. Tech. Phys-U (USA)* **17**, 329 (1972)
9. T.H. Demetrakopoulos, R. Mittra, Digital and optical reconstruction of images from suboptical diffraction patterns. *Appl. Opt.* **13**, 665 (1974)
10. L. Onural, P.D. Scott, Digital decoding of in-line holograms. *Opt. Eng.* **26**, 1124 (1987)
11. G. Liu, P.D. Scott, Phase retrieval and twin-image elimination for in-line Fresnel holograms. *J. Opt. Soc. Am. A* **4**, 159 (1987)

12. L. Onural, M.T. Oezgen, Extraction of three-dimensional object-location information directly from in-line holograms using Wigner analysis. *J. Opt. Soc. Am. A* **9**, 252 (1992)
13. H.J. Kreuzer, R.P. Pawlitzek, LEEPS, Version 1.2, A software package for the simulation and reconstruction of low energy electron point source images and other holograms (1993–1998)
14. H.-W. Fink, Point source for electrons and ions. *IBM J. Res. Dev.* **30**, 460(1986)
15. H.-W. Fink, Point source for electrons and ions. *Phys. Scripta* **38**, 260 (1988)
16. W. Stocker, H.-W. Fink, R. Morin, Low-energy electron and ion projection microscopy. *Ultra-microscopy* **31**, 379 (1989)
17. H.-W. Fink, W. Stocker, H. Schmid, Holography with low-energy electrons. *Phys. Rev. Lett.* **65**, 1204(1990)
18. H.-W. Fink, H. Schmid, H.J. Kreuzer, A. Wierzbicki, Atomic resolution in lens-less low-energy electron holography. *Phys. Rev. Lett.* **67**, 15(1991)
19. H.J. Kreuzer, K. Nakamura, A. Wierzbicki, H.-W. Fink, H. Schmid, Theory of the point source electron microscope. *Ultramicroscopy* **45**, 381 (1992)
20. H.-W. Fink, H. Schmid, H.J. Kreuzer, In: *Electron Holography*, eds. by A. Tonomura, L.F. Allard, D.C. Pozzi, D.C. Joy, Y.A. Ono, *State of the Art of Low-Energy Electron Holography*, (Elsevier, Amsterdam, 1995), pp. 257–266
21. H.-W. Fink, H. Schmid, E. Ermantraut, and T. Schulz, Electron holography of individual DNA molecules, *J. Opt. Soc. Am. A* **14**, 2168 (1997)
22. A. Götzhäuser, B. Völkel, B. Jäger, M. Zharnikov, H.J. Kreuzer, M. Grunze, Holographic imaging of macromolecules. *J. Vac. Sci. Technol. A* **16**, 3025 (1998)
23. H. Schmid, H.-W. Fink, H.J. Kreuzer, In-line holography using low-energy electrons and photons; applications for manipulation on a nanometer scale. *J. Vac. Sci. Technol. B* **13**, 2428 (1995)
24. H.J. Kreuzer, H.-W. Fink, H. Schmid, S. Bonev, Holography of holes, with electrons and photons. *J. Microsc.* **178**, 191 (1995)
25. H.J. Kreuzer, Low energy electron point source microscopy. *Micron* **26**, 503 (1995)
26. H.J. Kreuzer, N. Pomerleau, K. Blagrove, M.H. Jericho, Digital in-line holography with numerical reconstruction. *Proc. SPIE* **3744**, 65 (1999)
27. M. Born, E. Wolf. *Principles of Optics* (Cambridge University Press, Cambridge, 2006)
28. J. Garcia-Sucerquia, W. Xu, S.K. Jericho, M.H. Jericho, P. Klages, H.J. Kreuzer. Digital in-line holographic microscopy. *Appl. Opt.* **45**, 836–850 (2006)
29. J. Garcia-Sucerquia, W. Xu, S.K. Jericho, M.H. Jericho, P. Klages, H.J. Kreuzer. Resolution power in digital holography, in *ICO20: Optical Information Processing*; Y. Sheng, S. Z. Y. Zhang (eds.), *Proc. SPIE* **6027**, 637–644 (2006)
30. S.K. Jericho, J. Garcia-Sucerquia, Wenbo Xu, M.H. Jericho, H.J. Kreuzer. A submersible digital in-line holographic microscope. *Rev. Sci. Instr.* **77**, 043706 1–10 (2006)
31. H.J. Kreuzer, M.H. Jericho, Wenbo Xu, Digital in-line holography with numerical reconstruction: three-dimensional particle tracking. *Proc. SPIE* **4401**, 234, 2001
32. W. Xu, M.H. Jericho, I.A. Meinertzhagen, H.J. Kreuzer, Tracking particles in 4-D with in-line holographic microscopy. *Opt. Lett.* **28**, 164 (2003)
33. H.J. Kreuzer, M.H. Jericho, I.A. Meinertzhagen, W. Xu, Digital in-line holography with numerical reconstruction: 4D tracking of microstructures and organisms. *Proc. SPIE* **5005–17**, 299 (2003)
34. J. Garcia-Sucerquia, W. Xu, S.K. Jericho, M.H. Jericho, I. Tamblyn, H.J. Kreuzer, Digital in-line holography: 4-D imaging and tracking of micro-structures and organisms in microfluidics and biology, in *ICO20: Biomedical Optics*, G. von Bally, Q. Luo (eds.), *Proc. SPIE* **6026**, 267–275 (2006)
35. J. Garcia-Sucerquia, W. Xu, S.K. Jericho, M.H. Jericho, H.J. Kreuzer, Digital in-line holography applied to microfluidic studies, in *Microfluidics, BioMEMS, and Medical Microsystems IV*; I. Papautsky, W. Wang (eds.), *Proc. SPIE* **6112**, 175–184 (2006)
36. J. Garcia-Sucerquia, W. Xu, S.K. Jericho, M.H. Jericho, H.J. Kreuzer, 4-D imaging of fluid flow with digital in-line holographic microscopy. *Optik* **119**, 419–423 (2008)

37. J. Garcia-Sucerquia, D. Alvarez-Palacio, J. Kreuzer. Digital In-line Holographic Microscopy of Colloidal Systems of Microspheres, in Adaptive Optics: Analysis and Methods/Computational Optical Sensing. Meetings on CD-ROM OSA Technical Digest (CD) (Optical Society of America, 2007), paper DMB4
38. Wenbo Xu, M.H. Jericho, I.A. Meinertzhagen, H.J. Kreuzer, Digital in-line holography for biological applications. *Proc. Natl. Acad. Sci. USA* **98**, 11301 (2001)
39. N.I. Lewis, A.D. Cemballa, W. Xu, M.H. Jericho, H.J. Kreuzer, Effect of temperature in motility of three species of the marine dinoflagellate *Alexandrium*, in: Ed. by Bates, S.S. Proceedings of the Eighth Canadian Workshop on Harmful Marine. *Algae. Can. Tech. Rep. Fish. Aquat. Sci.* 2498: xi + 141, pp. 80–87 (2003)
40. N.I. Lewis, A.D. Cemballa, W. Xu, M.H. Jericho, H.J. Kreuzer. Swimming speed of three species of the marine dinoflagellate *Alexandrium* as determined by digital in-line holography. *Phycologia* **45**, 61–70 (2006)
41. L. Repetto, E. Piano, C. Pontiggia. Lensless digital holographic microscope with light-emitting diode illumination. *Opt. Lett.* **29** (10), 1132–1134 (2004)
42. J. Garcia-Sucerquia, D. Alvarez-Palacio, H.J. Kreuzer, Partially coherent digital in-line holographic microscopy. OSA/DH/FTS/HISE/NTM/OTA (2009).
43. P. Petruck, R. Riesenberger, M. Kanka, U. Huebner, Partially coherent illumination and application to holographic microscopy, in 4th EOS Topical Meeting on Advanced Imaging Techniques Conference 2009, pp. 71–72, (2009)
44. P. Petruck, R. Riesenberger, R. Kowarschik, Sensitive measurement of partial coherence using a pinhole array, in Proceedings OPTO Sensor+Test', pp. 35–40 (2009)
45. M. Kanka, R. Riesenberger, H.J. Kreuzer, Reconstruction of high-resolution holographic microscopic images. *Opt. Lett.* **34** (8), 1162–1164 (2009). doi:10.1364/OL.34.001162
46. M. Kanka, A. Wuttig, C. Graulig, R. Riesenberger, Fast exact scalar propagation for an in-line holographic microscopy on the diffraction limit. *Opt. Lett.* **35**(2), 217–219 (2010)
47. R. Riesenberger, M. Kanka, J. Bergmann, Coherent light microscopy with a multi-spot source, in T. Wilson, (ed.), *Proc. SPIE*, 66300I, (2007)
48. M. Kanka, R. Riesenberger, Wide field holographic microscopy with pinhole arrays, in Proceedings of OPTO Sensor+Test, pp. 69–72, (2006)
49. R. Riesenberger, A. Wuttig, Pinhole-array and lensless micro-imaging with interferograms, Proceedings of DGaO, 106. Conference, pp. A26, (2005)
50. A. Grjasnow, R. Riesenberger, A. Wuttig, Phase reconstruction by multiple plane detection for holographic microscopy, in T. Wilson, (ed.), *Proc. SPIE*, 66300J, (2007)
51. A. Grjasnow, R. Riesenberger, A. Wuttig, Lenseless coherent imaging by multi-plane interference detection, in Proceedings of DGaO, 106. Conference, pp. A39, (2005)
52. A. Grjasnow, A. Wuttig, R. Riesenberger, Phase resolving microscopy by multi-plane diffraction detection. *J. Microsc.* **231**(1), 115–123 (2008)
53. M. Heydt, A. Rosenhahn, M. Grunze, M. Pettitt, M.E. Callow, J.A. Callow, Digital in-line holography as a three-dimensional tool to study motile marine organisms during their exploration of surfaces. *J. Adhes.* **83**, 417–430 (2007)
54. M. Heydt, P. Divos, M. Grunze, A. Rosenhahn, Analysis of holographic microscopy data to quantitatively investigate three-dimensional settlement dynamics of algal zoospores in the vicinity of surfaces. *Eur. Phys. J.E.* **30**, 141–148 (2009)
55. A. Rosenhahn, S. Schilp, H.J. Kreuzer, M. Grunze, The role of inert surface chemistry in marine biofouling prevention. *Phys. Chem.Chem. Phys.* **12**, 4275–4286 (2010). doi: 10.1039/C001968M
56. H.J. Kreuzer, *Holographic microscope and method of hologram reconstruction* US. Patent 6411406 B1, (Canadian patent CA 2376395) 25 June, (2002)
57. DIHM software package, copyright Resolution Optics Inc. Halifax, see also resolutionoptics.com for further information
58. S.K. Jericho, P. Klages, J. Nadeau, E.M. Dumas, M.H. Jericho, H.J. Kreuzer, In-line digital holographic microscopy for terrestrial and exobiological research, *Planetary and Space Science* **58**, 701–705 (2010)

Coherent Light Microscopy

Imaging and Quantitative Phase Analysis

(Eds.) P. Ferraro; A. Wax; Z. Zalevsky

2011, XVI, 372 p. With online files/update., Hardcover

ISBN: 978-3-642-15812-4